Effect of pH and Temperature on the Morphology and Phases of Co-precipitated Hydroxyapatite

H. R. Le[a*], K. Y. Chen[b], C. A. Wang[b]

[a] School of Marine Science and Engineering, University of Plymouth, Plymouth PL4 8AA, United Kingdom

[b] Department of Materials Science & Engineering, Tsinghua University, Beijing 10084, P. R. China.

* Corresponding Author (H. R. Le): Tel: +44 1752 586172, Fax: +44 1752 586101, Email: huirong.le@plymouth.ac.uk

Abstract

This paper reports a high-yield process to fabricate biomimetic hydroxyapatite nano-particles or nano-plates. Hydroxyapatite is obtained by simultaneous dripping of calcium chloride ($CaCl_2$) and ammonium hydrogen phosphate $(NH_4)_2HPO_4$ solutions into a reaction vessel. Reactions were carried out under various pH and temperature conditions. The morphology and phase composition of the precipitates were investigated using scanning electron microscope (SEM) and X-ray diffraction (XRD). The analyses showed that large plates of calcium hydrophosphate are formed at neutral or acidic pH condition. Nanoparticles of hydroxyapatite were obtained in precipitates prepared at pH 9 to 11. Hydroxyapatite plates akin to seashell nacre were obtained at 40°C and pH 9. This material holds promise to improve the strength of hydroxyapatite containing composites for bone implant or bone cement used in orthopaedic surgeries. The thermodynamics of the crystal growth under these conditions was discussed. An assembly mechanism of the hydroxyapatite plates was proposed according to the nanostructure observations.

Keywords: Biomimetic, Hydroxyapatite, Co-precipitation, Nanoplate.

1. INTRODUCTION

The demand for artificial bone replacement is growing in the last few decades. Metals such as titanium alloys and stainless steel are used to fix major bone damages. However, when the alloys of metals are implanted into the body, toxic elements may diffuse into the bone tissue, resulting in further complications. Under high stress areas the metallic implants can damage or even rip apart the surrounding healthy tissues inside the body. It has been reported that stainless steel and titanium alloy implants can cause inflammatory effects due to leached toxic ions such as nickel, cobalt, chromium, aluminium and vanadium. Even the bioinert alumina and zirconia ceramics suffer such issues due to mechanical mismatch. All these limiting factors that prevail in these procedures call for more advanced bone replacement materials. Such a material should be biocompatible, should also be strong enough to support the fractured bone and withstand strain under pressure.

There is considerable interest in biomimetic bone replacement materials under the premise that a material with similar composition and structure to bone should be biocompatible. It is well known that hydroxyapatite and collagen are the main compositions of natural bone tissues. Collagen is the most commonly found protein in musculoskeletal system, which forms the extra cellular matrices such as tendons, ligaments, skins and scar tissues in vertebrates and it accounts for 17%-20% of the total mass of natural bones [1]. The naturally occurring collagen in the body possesses a good tensile strength considered as 'steel' in human body because it is the load carrying component not only in bones, but also for blood, muscles and tendons [2-3]. Hydroxyapatite is the mineral component of bone tissues which account for 69%-80% of the mass of the bones and teeth. Natural hydroxyapatite crystals are usually of rod-like structures that assemble on collagen fibres with varying proportions. The resulting structure exhibits cross-linked patterns to form mechanically strong tissues [1]. Previous research indicated that synthetic hydroxyapatites and collagen nanocomposites are bioactive as they support bone ingrowth and osteointegration [4-8]. The bioactivity can be further improved by incorporating carbonate, chloride and fluoride hydroxyl groups into hydroxyapatite structure. The ability of hydroxyapatite to integrate into natural bones and support bone growth without breaking or dissolving has been the key criteria to be chosen for bone substitutes [5-6]. Synthetic hydroxyapatite is also used as a scaffold material for bone tissue engineering or bioactive coating for titanium implants [9-10].

Hydrothermal precipitation process is most widely used to fabricate hydroxyapatite and its nanocomposites. The effects of precursors, concentrations, pH, temperature and surfactants have been studied. The kinetics of hydroxyapatite precipitation from aqueous solution at the conditions of pH10 to 11 involves the formation of intermediate octacalcium phosphate, amorphous calcium phosphate and transformation to hydroxyapatite [11]. The reaction temperature has significant effect on the phase transformation and morphology of precipitated hydroxyapatite. Liao et al [12] used calcium chloride ($CaCl_2$) and phosphoric acid (H_3PO_4) for the fabrication of hydroxyapatite/collagen composite. Another paper reports the use of calcium chloride ($CaCl_2$) and sodium hydrogen phosphate (NaH_2PO_4) as reagents for the fabrication [13]. Several other papers describe the reaction of calcium hydroxide ($Ca(OH)_2$) with phosphoric acid (H_3PO_4) for the fabrication of hydroxyapatite composites [14-15]. The morphology of the hydroxyapatite nanocrystals obtained from hydrothermal route can be controlled by the pH, temperature conditions and surfactants [16-19]. It has been reported that the rise in pH, temperature and the addition of surfactants increases anisotropic growth and hence increase the crystal aspect ratio. However, sodium tripolyphosphate acts as a growth inhibitor by combining with calcium ions and hence promotes the growth of plates [20].

Hydrothermal process requires very low concentration of solutions and a long time of incubation to develop nanostructured hydroxyapatite. The yield is small due to the low concentrations required of precursors. This paper will employ a different fabrication process in which both calcium containing and phosphate containing precursor solutions are dripped into reaction vessel gradually under various temperature and pH. The concentration of the calcium and phosphate ions will remain fairly constant in the reaction vessel while calcium phosphate is precipitated. Because higher concentration of precursor solutions can be used, this process is more efficient particularly at elevated temperature. It is expected that the morphology of hydroxyapatite will be different from that produced by instantaneous mixing of two solutions in sol-gel process.

2. Materials and Methods

2.1 Material preparation

The process of the co-precipitation reaction process is shown in Fig. 1. Both calcium chloride ($CaCl_2$) and ammonium hydrogen phosphate ((NH_4)$_2HPO_4$) solutions were dripping simultaneously into the reaction vessel. The solution in the reaction vessel was constantly stirred using a magnetic stirrer to maintain constant temperature and to expedite the reaction. In order to maintain constant calcium to phosphor ratio at 5:3 as in the formula of Ca_{10} (PO_4)$_6$(OH)$_2$, calcium chloride solution was diluted to 0.2mol/litre and ammonium hydrogen phosphate to 0.12mol/litre. The solutions were dripped at roughly equal rates using valve controlled burettes. Initial reactions were carried out without pH control; for example 100ml of $CaCl_2$ solution and 100ml of (NH_4)$_2HPO_4$ solution were dropped into 50ml of deionised (DI) water in the reaction vessel within one hour. The final pH value is about 4 after the two solutions are fully mixed. Once the reactions were completed, each of the formed precipitate was titrated to various pH using 0.5 mol/litre NaOH solution and then placed in a water bath aging at corresponding temperature for 24 hrs. Six precipitates (numbered a to f) were prepared at two temperatures, 20 or 40 ˚C, and aged at three different pH levels, pH7/pH9/pH11. Additional four samples (numbered g to j) were prepared with pH control during precipitation. The pH in the reaction vessel was titrated frequently to 7, 9 or 11 respectively during the reaction. The reaction vessel would then be moved to a water bath when reaction was complete and kept for 24 hours at the corresponding reaction temperature.

After 24 hours of aging, each precipitate was then filtered using vacuum assisted filtering to remove excess water and free ions. Once the excess water was removed from the filter, the next step was to rinse the precipitates using DI water for several times. Water dissolvable ions were removed from the deposit including chloride ions (Cl^-), sodium ions (Na^+) and ammonium ions (NH_4^+). After vacuum assisted filtering, the precipitates were dried in vacuum oven at corresponding temperature. The paste became solid blocks which can be observed under SEM or tested by XRD.

2.2 XRD phase and microstructural analysis

The phase constituents of each precipitate were examined using XRD. Certain amount of precipitate was ground into powder and then pressed into flat sample. X-ray powder diffraction patterns were measured on Rigaku D/max2500 X-ray diffractometer with Cu Kα radiation at a scanning speed of 6°/min in range of 10° to 80°. The operating voltage and current of this XRD machine were 40 kV and 200 mA, respectively. The phases of each precipitate were determined by comparing the XRD patterns with JCPDF database.

Scanning electron microscopes (SEM) were used for studying the morphology of the precipitates fabricated. The machines used were JSM-6460 SEM (Tsinghua) and Philips XL 30 ESEM (Dundee). The samples were mounted on aluminium stubs. The surface of the stub had carbon adhesives which hold the samples in place. Then these stubs were moved into a sputter coater. The dried blocks were coated with Gold/ Palladium up to 30 nm of thickness in order to dissipate the fast impinging electrons on the specimens during SEM operation.

3. Results

3.1 Morphology and phase composition without pH control during precipitation

SEM images allow an in-depth view of the structure of the precipitates described above. Fig. 2 is showing the microstructure of samples precipitated at 20 ˚C without pH control but aged under pH7 or pH9. There are two distinctive morphologies: large plates and clusters of nano-particles. The width of the plates is as large as 10 to 20 μm with a thickness of about 400 nm. The dimensions are similar to seashell nacre. Fig. 3 is showing the morphology of precipitates made at 40˚C without pH control. When aged at pH 7 (c.f. Fig. 3a), the main feature is the clusters of nano-particles with a small fraction of plates. When the aging pH is raised to 9, the plates disappear (Fig. 3b). Fig. 4 is showing the morphology of the precipitates aged at pH 11. The morphology exhibits clusters of nano-particles when aged at 20˚C or bundles of acicular crystals aged at 40˚C.

XRD patterns, as shown in Fig. 5, indicated that the precipitates aged under pH7/20˚C, pH7/40˚C or pH9/20˚C are a mixture of calcium hydrophosphate ($CaHPO_4 \bullet 2H_2O$, abbreviated CHP, JCPDF720713) and hydroxyapatite (JCPDF740566, abbreviated HA). The peaks of hydroxyapatite are apparently widened which are typical of nanoparticles. The precipitates aged at pH9/40˚C or those aged at pH11 are predominantly hydroxyapatite particles. This is inferring that the large plates present in the precipitates are the calcium hydrophosphate crystals while the nanoparticles are hydroxyapatite. The formation of calcium hydrophosphate is owing to the acidic condition during precipitation. It was then decided to control the pH value during precipitation.

3.2 Morphology and phase composition with pH control during precipitation

The effect of pH control during precipitation on the morphology was investigated. The suspension in the reaction vessel was titrated regularly during precipitation using NaOH solution to desired pH value. The precipitated was then aged in water bath under the same temperature. Fig. 6 is showing the morphology of precipitates prepared with pH control. The precipitate prepared at pH 7/20˚C is a mixture of plates and globules of nano-particles, but the fraction of plates is smaller compared to that precipitated without pH control (c.f. Fig. 6a). No plates are found in the precipitate prepared at pH9/20˚C (c.f. Fig 6b). The granules are of the size ranging from few nanometres to 15 nm. It is thought that the nucleation rate of the hydroxyapatite crystals is faster at pH9 than at pH7 so that more particles are formed, the nuclei of crystals grow slower due to the low temperature and become nano particles [11].

XRD analysis (Fig. 7) showed that precipitate prepared and aged at pH7/20˚C consists of CHP and HA. This is consistent with the SEM observation that there are plates (CHP) and granules (HA). The precipitates prepared at pH 9 to 11 are predominantly HA nano particles.

The morphology of the hydroxyapatite crystals obtained at pH9/40˚C is shown in Fig. 8. The precipitate consists of interlocked plates as well as scattered nano-particles. The width of the plates is about 1-2 μm and the thickness about 80 nm. A closer view of the plates shown in Figures 8b and 8c indicate that the hydroxyapatite plates are formed by assembled nano-particles (c.f. Fig. 8b) or nano-rods (c.f. Fig. 8c). The morphology is akin to the nanostructure of aragonite crystals in seashell nacre which exhibit nanoscale pattern on the plate surface. It is believed that the nanostructure of the surface is responsible for the superior toughness of seashell nacre [21-22]. The formation of plates of hydroxyapatite indicates that acicular crystals of hydroxyapatite are initially nucleated. Planar assembly of acicular crystals is favoured during precipitation process under these conditions. It is envisaged that this nanoplate structure could improve the stiffness and strength of hydroxyapatite nanocomposite bone grafts or scaffolds for bone tissue engineering [22].

4. Discussions

4.1 Thermodynamics analysis of primary crystal growth

Table1. Effects of Precipitation Conditions on Morphology and Phase Composition

No	pH at precipitation	pH at aging	Temp (C)	SEM	XRD
a	No control	7	20	Mainly large plates	CHP[a] & HA[b]
b	No control	7	40	Large plates and powder	CHP & HA
c	No control	9	20	Mainly large plates	CHP & HA
d	No control	9	40	Mainly powder	HA
e	No control	11	20	Mainly powder	HA
f	No control	11	40	Mainly powder	HA
g	7	7	20	Powder & large plates	CHP+HA
h	9	9	20	Mainly powder	HA
i	11	11	20	Mainly powder	HA
j	9	9	40	Assembled nanoplates	HA

[a]$CaHPO_4 \cdot 2H_2O$ (JCPDF720713)
[b]$Ca_{10}(PO_4)_6(OH)_2$ (JCPDF740566)

Table 1 summarises the observations of morphology and the phase analysis. The results indicate that increasing the pH and/or the temperature will favour the formation of hydroxyapatite. This is in line with the driving force analysis proposed by Viswanath and Ravishankar [15]. In this process, the solutions are gradually mixed in the reaction vessel. The concentrations of the ions are difficult to estimate. As a first approximation, it is assumed that the solutions are mixed immediately. In the reaction vessels the concentration of $Ca(NO_3)_2$ will be 0.066mol/litre, $(NH_4)_2HPO_4$ will be 0.04mol/litre. The ionic activity strength for HA can be derived as:

$$IAP = a^5\left(Ca^{2+}\right)a^3\left(PO_4^{\,2-}\right)a\left(OH^-\right) = 8.649 \times 10^{-52}\frac{\left[OH^-\right]}{\left[H^+\right]^3}, \tag{1}$$

which can be rewritten in terms of pH value:

$$\log(IAP) = 4pH - 65.06. \tag{2}$$

The solubility product of HA can be expressed by the following equation:

$$\log(K_{sp}) = -8219.41/T - 1.6657 - 0.0982157T. \tag{3}$$

Finally free energy change for the precipitation of HA is given by:

$$\Delta G = -RT/v \; \ln\left(IAP/K_{sp}\right) = -8.508 pH * T + 134.78T - 17482.68 - 0.2089T^2 \tag{4}$$

Fig. 10 shows the morphology diagram on a pH-T plot. The constant driving force lines correspond to $\Delta G=0$ (equilibrium), ΔG_{2D}= - 6.59kJ/mol (critical driving force for layer-by-

layer growth) and ΔG_{3D}= - 20.69 kJ/mol (critical driving force for continuous growth). Compared to the diagram of Viswanath and Ravishankar [15], the constant driving force lines are lower due to higher concentrations of solutions in current programme. The two experimental points at pH 11 are above ΔG_{3D} which means the crystals tend to grow in 3D. This is confirmed by SEM image in Fig. 4. The four experimental points at pH7 and 9 fall in between ΔG_{2D} and ΔG_{3D} which is the transition region from 2D to 3D. The crystals deposited under these conditions tend to retain plate-like structure as shown in Figs. 6 & 8. Crystals deposited at 20°C without pH control shown in Figs. 2(a) and (b) retain large calcium hydrophosphate plates even after aging 24 hours. This is because the pH drops to about 4 when two solutions are mixed which lead to the formation of calcium hydrophosphate. Phase transformation from solid to solid will require much higher driving force. When aging pH is increased to 11 (c.f. Fig. 2(c)) or temperature increased to 40 °C (Fig. 3), phase transformation into hydroxyapatite occurs because the driving force increases.

4.2 Plate-like grain growth mechanism

The nanostructure of the hydroxyapatite plates shown in Figs. 8 and 9 indicates that the primary precipitation of hydroxyapatite is nanorods or nanoparticles. The nanorods are grown in c-axis because the XRD spectrum showed that (002) peak at about 26° is sharper than other peaks. The nanorods tend to grow into plates as shown in Fig. 11. This can be called secondary growth because it happens after the primary precipitation. The main driving force of this is the reduction in surface energy due to the reduction in solid-liquid surface of the nanorods. The reduction in Gibbs energy can be derived as:

$$\Delta G = A_i (\gamma_{GB} - 2\gamma_{SL}), \tag{5}$$

where A_i is the total grain boundary area generated, γ_{GB} is the grain boundary energy between nanorods, γ_{SL} is the surface energy of nanorod in solution. It is believed that (100) face of nanorods has larger surface energy (γ_{SL}) than other faces as found by Zhang et al [19]. Therefore side-by-side contact will have larger driving force than end-to-end contact. Further, parallel packing is preferred because it will maximize the contact area A_i and hence reduce the total surface energy. The electron microscope images (c.f. Figs. 8 & 9) also show that each plate consists of very limited number of layers of nanorods. This is because the orientation of adjacent nanorods will be more distorted with increasing number of layers which will increase the grain boundary energy (γ_{GB}) of the plate and hence reduce the grain growth driving force.

5. Conclusions

(1) A high-yield precipitation reaction process was developed to fabricate hydroxyapatite using calcium chloride ($CaCl_2$) and ammonium hydrogen phosphate (($NH_4)_2HPO_4$) solutions as precursors. The reactions were carried out with or without pH control during precipitation and the precipitates aged at various pH and temperature conditions.

(2) The SEM images showed that large plates are present when the pH is not controlled during precipitation so that it becomes acidic. The plates disappear when pH is above 9 during precipitation. The presence of large plates is coincided with the presence of calcium hydrophosphate (JCPDF720713) in XRD patterns. It is inferred that the large plates are calcium hydrophosphate formed under acidic pH.

(3) Under desirable pH and temperature conditions hydroxyapatite nanoplates are formed. The plates are formed by planar assembly of nanoparticles or nanorods with a width of about 1-2 μm and a thickness of about 80nm. The surface topography of the plates resembles that of aragonite minerals in seashell nacre. This provides a new nanomaterial for fabrication of artificial nacre which is bioactive and holds promise to improve the strength of biomaterials for bone implant or bone scaffolds.

References

[1] Meyers M A, Chen P-Y, Lin A Y, Seki Y(2008) Biological materials: Structure and mechanical properties. Progress in Materials Science 53: 1-206.

[2] Gentleman E, Lay AN, Dickerson DA, Nauman EA, Livesay GA, K. Dee C (2003) Mechanical characterization of collagen fibers and scaffolds for tissue engineering. Biomaterials 24: 3805–3813.

[3] Yana J, Daga A, Kumar R, Mecholsky JJ (2008) Fracture toughness and work of fracture of hydrated, dehydrated, and ashed bovine bone, Journal of Biomechanics 41: 1929–1936.

[4] Kikuchi M, Ikoma T, Itoh S, Matsumoto H, Koyama Y, Takakuda K, Shinomiya K, Tanaka J (2004) Biomimetic synthesis of bone-like nanocomposites using the self-organization mechanism of hydroxyapatite and collagen. Composites Science and Technology 64: 819-825.

[5] Kim H -W, Kim H –E, Salih V (2005) Stimulation of osteoblast responses to biomimetic nanocomposites of gelatin-hydroxyapatite for tissue engineering scaffolds. Biomaterials 26: 5221-5230.

[6] Kikuchi M, Itoh S, Ichinose S, Shinomiya K and Tanaka J (2001) Self Organisation Mechanism in Bone-Like Hydroxyapatite / Collagen Nanocomposite Synthesized in Vitro and its Biological Reaction in Vivo. Biomaterials 22: 1705-1711.

[7] Kikuchi M, Matsumoto HN, Yamada T, Koyama Y, Takakuda K and Tanaka J (2004) Glutaraldehyde Cross-Linked Hydroxyapatite/Collagen Self-Organized Nanocomposites. Biomaterials 25: 63-69.

[8] Zhang W, Liao SS, Cui FZ (2003) Hierarchical Self-Assembly of Nano-Fibrils in Mineralised Collagen. Chemistry of Materials 15: 3221-3226.

[9] Manara S, Paolucci F, Palazzo B, Marcaccio M, Foresti E, Tosi G, Sabbatini S, Sabatino P, Altankov G, Roveri N (2008) Electrochemically-assisted deposition of biomimetic hydroxyapatite–collagen coatings on titanium plate. Inorganica Chimica Acta 361: 1634–1645.

[10] Muller FA, Muller L, Caillard D, Conforto E (2007) Preferred growth orientation of biomimetic apatite crystals, Journal of Crystal Growth 304: 464-471.

[11] Liu C, Huang Y, Shen W, Cui J (2001) Kinetics of hydroapatite precipitation at pH 10 to 11, Biomaterials 22: 301-306.

[12] Liao S, Ngiam M, Watari F, Ramakrishna S, Chan CK(2007) Systematic Fabrication of Nano-Carbonated Hydroxyapatite/Collagen composites for Biomimetic Bone Grafts. Bioinspiration & Biomimetics 2: 37-41.

[13]Rusu VM, Ng C –H, Wilke M, Tiersch B, Fratzl P and Peter M G (2005) Size-controlled hydroxyapatite nanoparticles as self-organized organic–inorganic composite materials, Biomaterials 26: 5414-5426.

[14]Yunoki S, Ikoma T, Monkawa A, Ohta K, Kikuchi M, Sotome S, Shinomiya K, Tanaka J (2006) Control of pore structure and mechanical property in hydroxyapatite/collagen composite using unidirectional ice growth. Materials Letters 60: 999–1002.

[15]Yoon B –H, Kim H –W, Lee S –H, Bae C –J, Koh Y –H, Kong Y–M, Kim H–E (2005) Stability and cellular responses to fluorapatite–collagen composites. Biomaterials 26: 2957–2963.

[16] Viswanath B, Ravishankar N (2008) Controlled synthesis of plate—shaped hydroxyapatite and implications for the morphology of the apatite phase in bone. Biomaterials 29: 4855-4863.

[17] Neira IS, Kolenko YV, Lebedev OL, Van Tendeloo G, Gupta HS, Guitian F, Yoshimura M (2009) An efficient morphology control of hydroxyapatite crystal via hydrothermal synthesis. Crystal Growth & Design 9: 466-474.

[18] Ma T, Xia Z, Liao L (2011) Effect of reaction systems and surfactant additives on the morphology evolution of hydroxyapatite nanorods obtained via a hydrothermal route. Applied Surface Science 257: 4384-4388.

[19] Rajkumar M, Sundaram NM, Rajendran V (2011) Preparation of size controlled, stoichiometric and bioresorbable hydroxyapatite nanorod by varying initial pH, Ca/P ratio and sintering temperature. Digest Journal of Nanomaterials and Biostructures 6: 169-179.

[20] Zhang H-B, Zhou K, Li Z, Huang S (2000) Plate-like hydroxyapatite nanoparticles synthesized by the hydrothermal method. J Physics and Chemistry of Solids 70: 243-248.

[21] Wang R Z, Suo Z, Evans AG, Yao N and Aksay I A (2001) Deformation mechanisms in nacre. J. Mater. Res. 16: 2485.

[22] Evans AG, Suo Z, Wang RZ, Aksay IA, He MY and Hutchinson JW (2001) Model for the robust mechanical behavior of nacre. J. Mater. Res. 16: 2475.

CaCl₂   (NH₄)₂HPO₄

Constant temperature and pH

Magnetic Stirrer
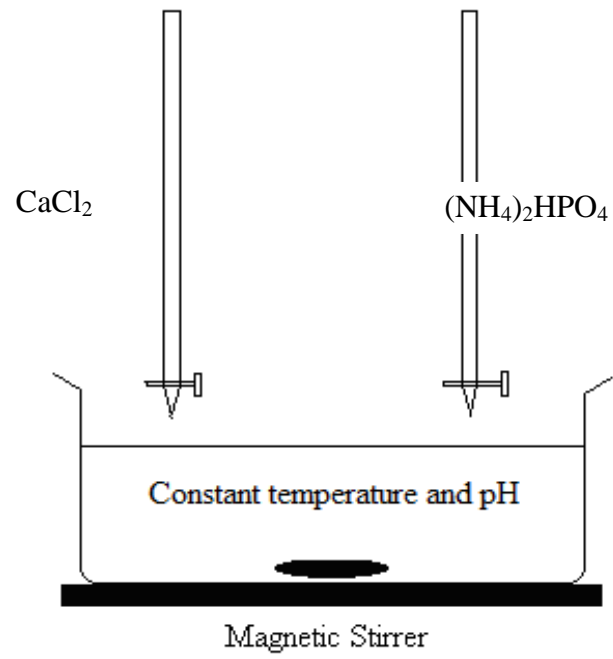
Figure 1 Precipitation reaction diagram

(a)

(b)
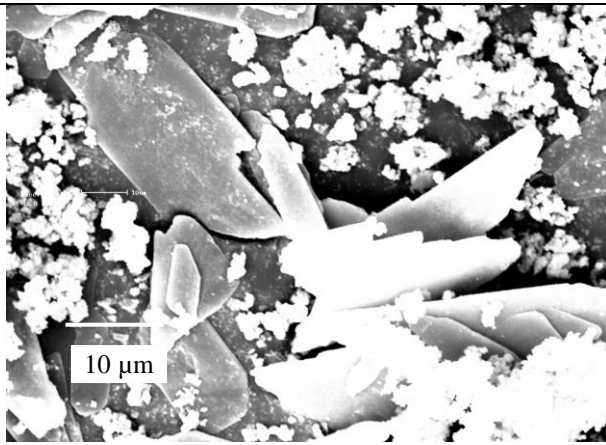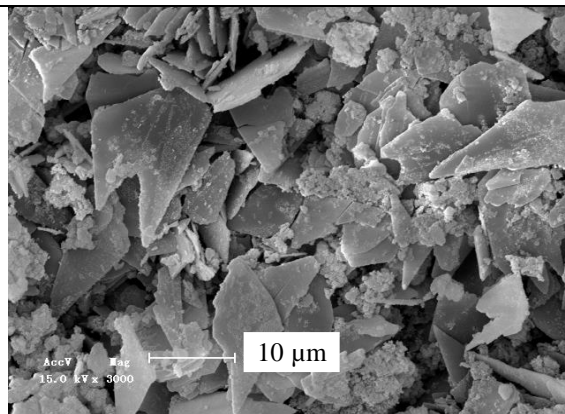
Figure 2 SEM images of precipitates prepared at 20˚C without pH control, (a) aged at pH 7, (b) aged at pH 9
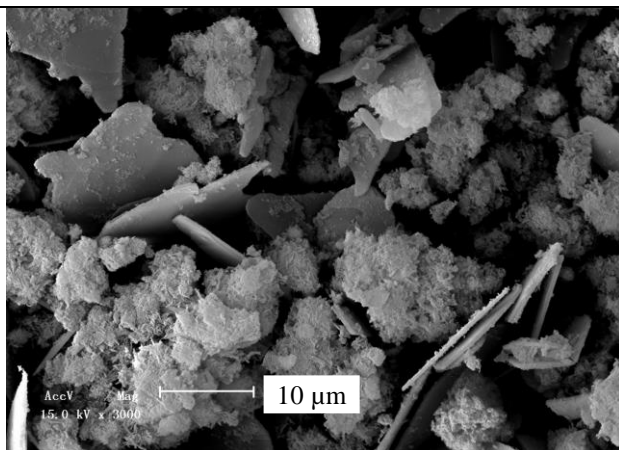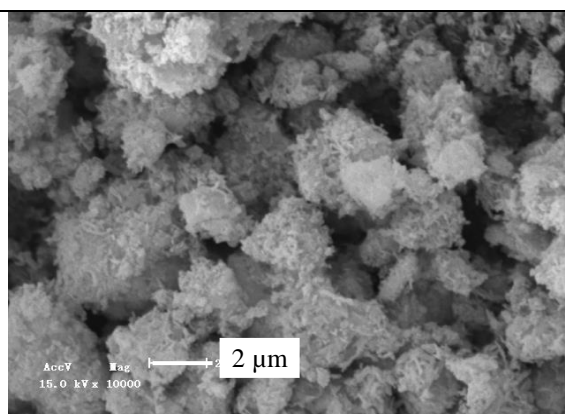
(a)
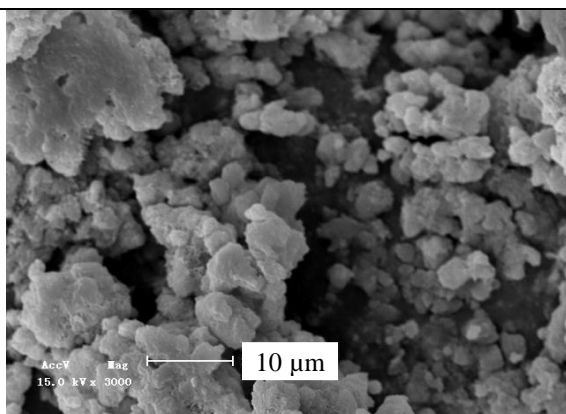
(b)

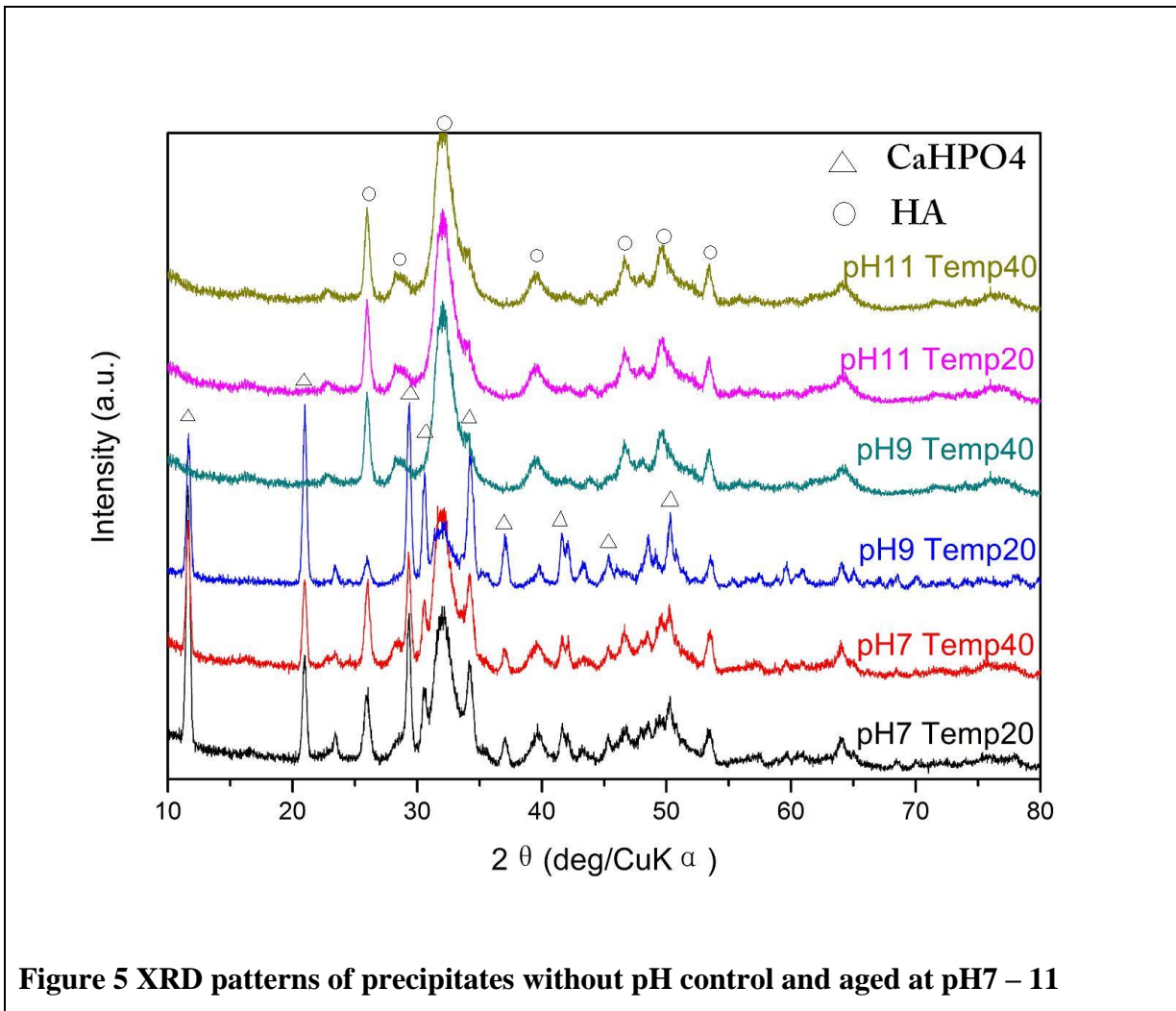**Figure 3 SEM images of precipitates prepared at 40˚C without pH control, (a) aged at pH 7, (b) aged at pH 9**
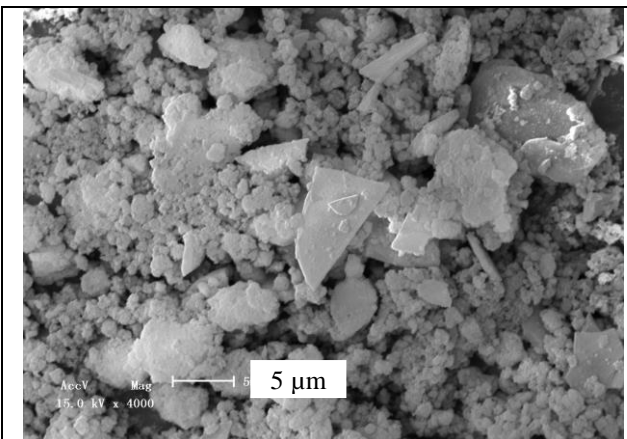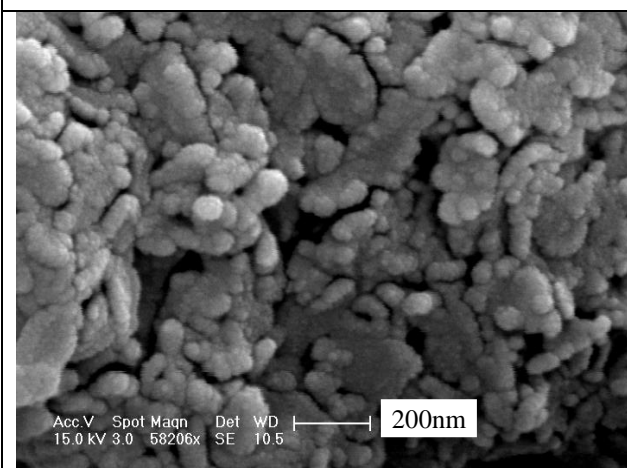
(a)

(b)
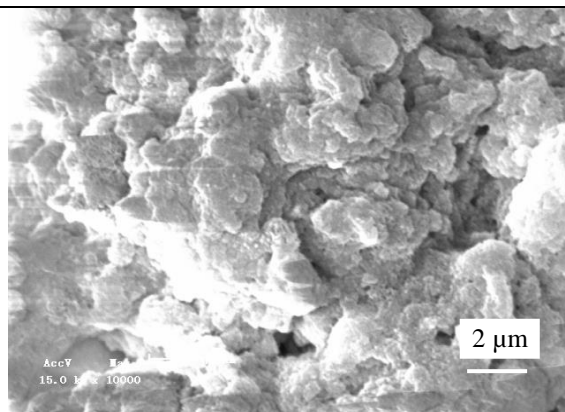
Figure 2 SEM images of precipitates prepared without pH control, (a) aged at 20 ˚C, pH 11, (b) aged at 40 ˚C, pH 11

Figure 5 XRD patterns of precipitates without pH control and aged at pH7 – 11

(a)

(b)

Figure 6 SEM images of precipitates prepared with pH control at (a) pH7 - 20°C and (b) pH9 - 20°C

Figure 7 XRD patterns of precipitates with pH control
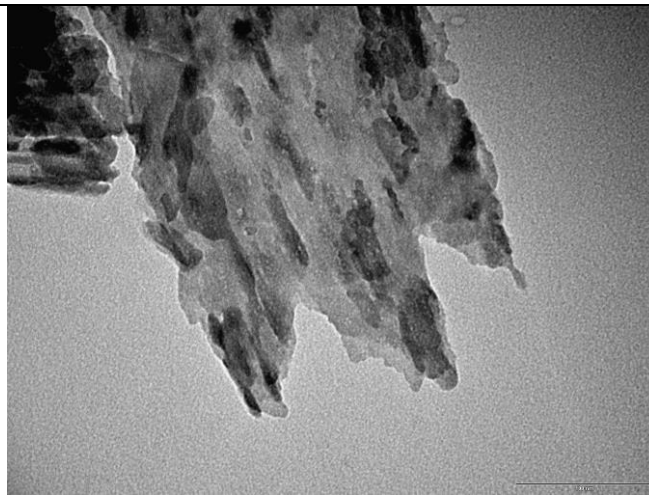
(a)

76.1 nm
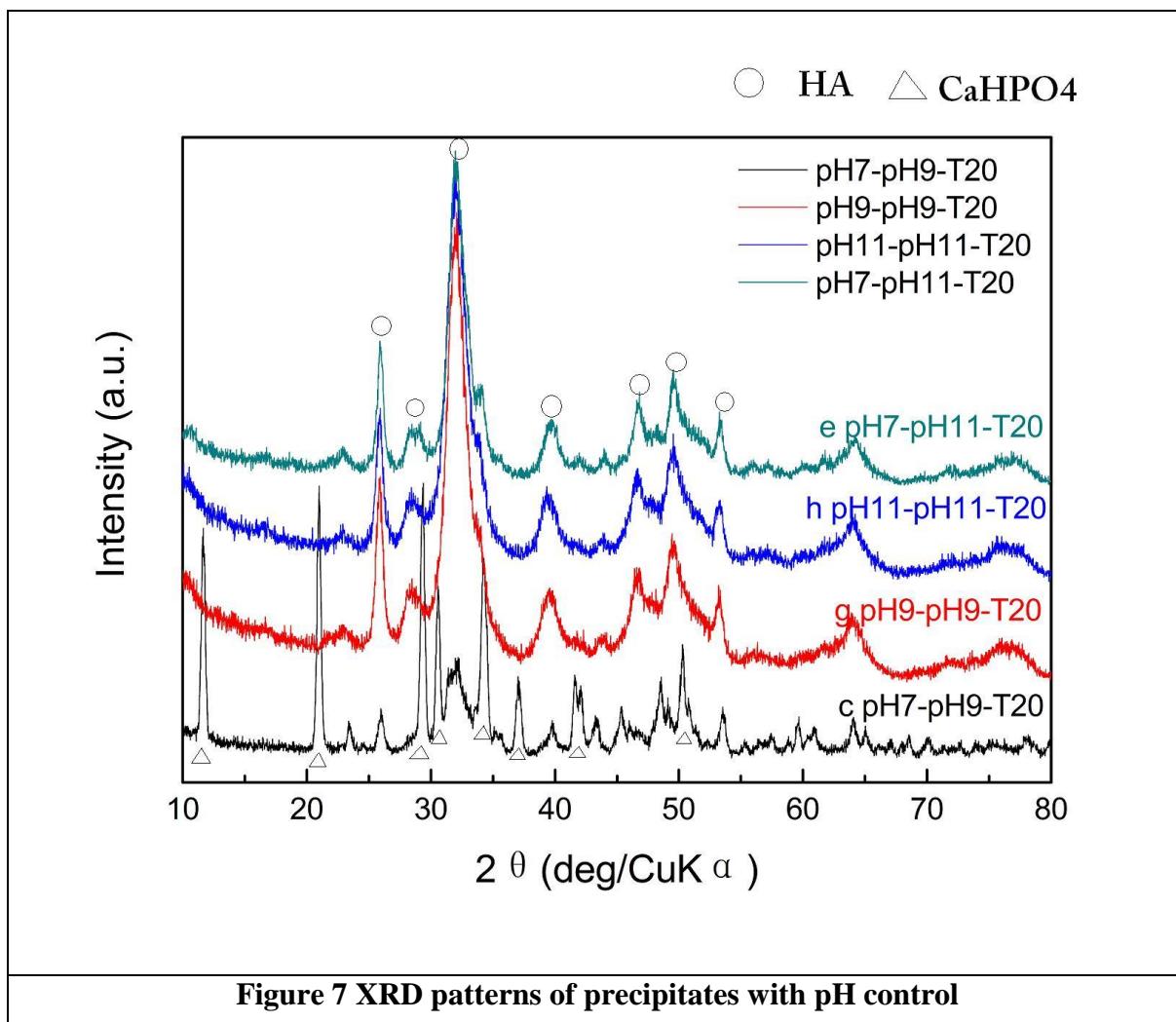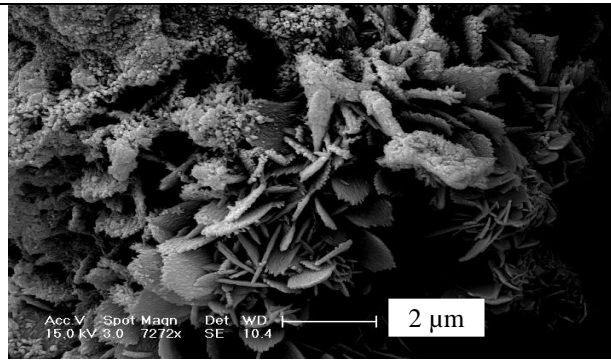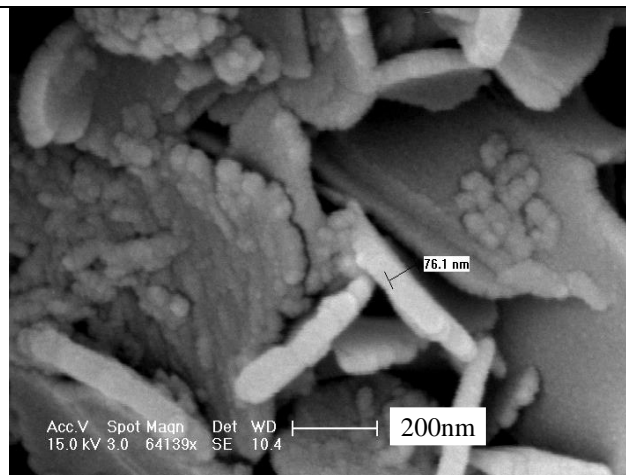
(b)
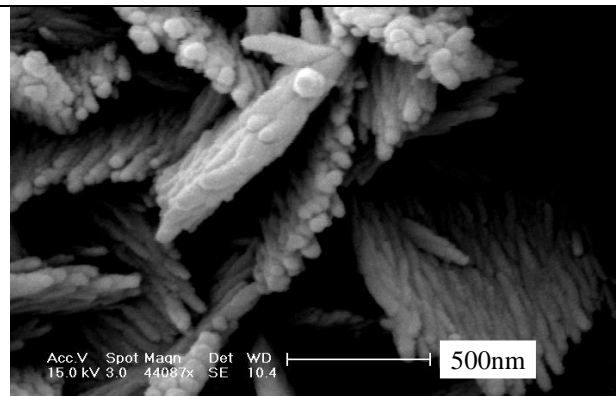
(c)

Figure 8 Hydroxyapatite nanoplates prepared at 40˚C and pH 9, (a) overview (b) nanoparticles assembled plates (c) nanorods assembled plates
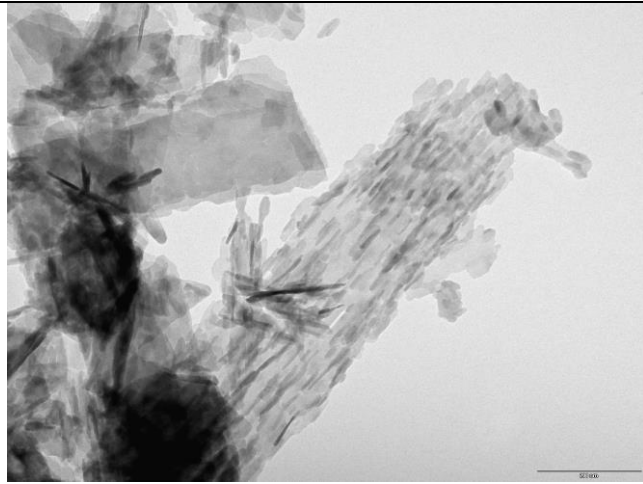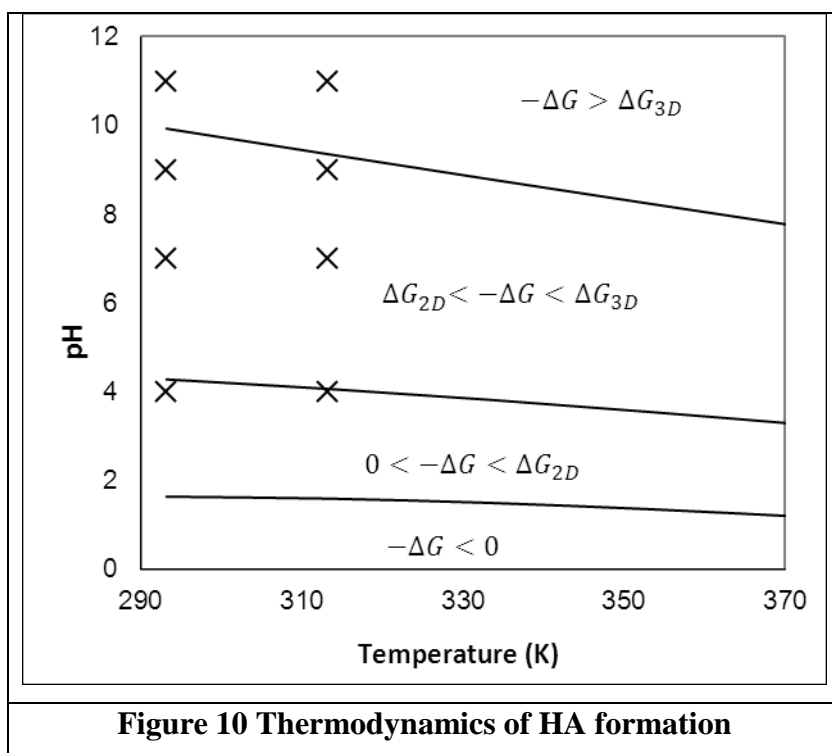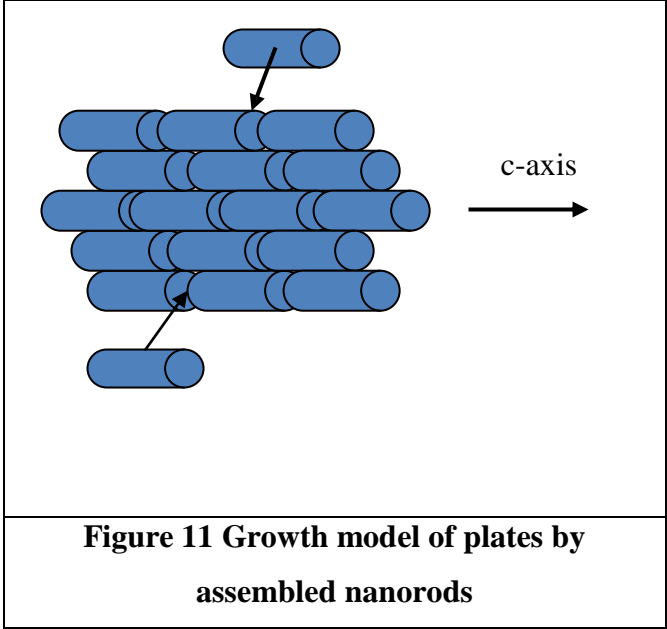
(a)

(b)

**Figure 9 TEM Hydroxyapatite nanoplates
prepared at 40°C and pH 9, (a) overview, (b)
nanorods assembled plates.**

Figure 10 Thermodynamics of HA formation

Figure 11 Growth model of plates by assembled nanorods